

Part One
Nanogels, Interfaces, Carriers, and Polymersomes

1

Towards Self-Healing Organic Nanogels: A Computational Approach

German V. Kolmakov, Solomon F. Duki, Victor V. Yashin and Anna C. Balazs

1.1 Introduction

The ability to heal wounds is one of the truly remarkable properties of biological systems. A grand challenge in materials science is to design “smart” synthetic systems that can mimic this behavior by not only “sensing” the presence of a “wound” or defect, but also actively re-establishing the continuity and integrity of the damaged area. Such materials would significantly extend the lifetime and utility of a vast array of manufactured items. Nanotechnology is particularly relevant to both the utility and fabrication of self-healing materials. For example, as devices reach nanoscale dimensions, it becomes critical to establish a means of promoting repair at these length scales. Whilst operating and directing minute tools to carry out this operation is still far from trivial, an optimal solution would be to design a system that could recognize the appearance of a nanoscopic crack or fissure, and then direct the agents of repair specifically to that site. Even in the manufacture of various macroscopic components, nanoscale damage is a critical issue. For instance, nanoscopic notches and scratches can appear on the surface of materials during the manufacturing process. Because of the small size of these defects they are difficult to detect and, consequently, difficult to repair. Such defects, however, can have a substantial effect on the mechanical properties of the system. For example, significant stress concentrations can occur at the tip of notches in the surface; such regions of high stress can ultimately lead to the propagation of cracks through the system and the degradation of mechanical behavior.

Thus, one of the driving forces for creating self-healing materials [1–9] is in fact the need to effect repair on the nanoscale. On the positive side, advances in nanotechnology could also provide routes for realizing the creation of these materials. In particular, scientists can now produce a stunning array of nanoscopic particles, and have become highly adept at tailoring the surface chemistry of the particles. In this chapter, recent computational studies on the design of self-healing materials that exploit the unique properties of *soft* nanoscopic particles are reviewed. As noted further below, these studies take their inspiration from biological systems that show remarkable resilience in response to mechanical deformation.

In a recent study [10], attention was focused on nanoscopic polymer gel particles, or “nanogels” [11], as the primary building blocks in the system. New methodologies have recently enabled the well-controlled synthesis of such colloids [12]. Furthermore, the surface of these particles can be functionalized with various reactive groups, which allow the individual nanogel particles to be cross-linked into a macroscopic material [11]. By using a coarse-grained computational model, it was possible to examine systems of such crosslinked, soft nanogel particles, and to design a coating that would undergo structural rearrangement in response to mechanical stress, and thus prevents any catastrophic failure of the material [10].

It was assumed that the particles were connected via a fraction of labile bonds (e.g., thiol, disulfide, or hydrogen bonds) [3]; the particles were also interconnected by stronger, less-reactive bonds (e.g., C–C, bonds)—referred to as “permanent” bonds—and thus, the system exhibits a so-called “dual crosslinking.” Within this system, the stable, “permanent” bonds between the nanogels play an essential role by imparting structural integrity. As discussed below, it is the reactive, labile bonds, however, that improve the strength of the material. In particular, when the material is strained, the labile bonds break before the stronger connections; these broken bonds then allow the particles to slip and slide, to come into contact with new neighbors, and to make new connections that maintain the continuity of the film. In this manner, the labile bonds can postpone catastrophic failure and, thereby, impart self-healing properties to the material. Through computer simulations, the parameter range was pinpointed for optimizing this self-healing behavior. In fact, it was found that only a relatively small volume fraction of labile bonds within the material could cause a dramatic increase in the ability of the network to resist catastrophic failure [10].

The above behavior is conceptually analogous to the properties that contribute to the strength of the abalone shell *nacre*, where brittle inorganic layers are interconnected by a layer of crosslinked polymers [13]. Under a tensile deformation, the weak crosslinks or “sacrificial bonds” are the first to break. These ruptures dissipate energy and thus mitigate the effects of the mechanical deformation. Consequently, the breakage of these sacrificial bonds helps to maintain the structural integrity of the material.

It should be mentioned that, in another recent study [14], inspiration was taken from nature; namely, the functionality of biological leukocytes, which localize at a wound and thereby facilitate the repair process. In the synthetic system, the “leukocyte” represents a polymeric microcapsule, the healing agents represent encapsulated solid nanoparticles, and the “wound” is a microscopic crack on a surface. In the simulation, the nanoparticle-filled microcapsules are driven by an imposed fluid flow to move along the cracked substrate. The goal was to determine how the release of the encapsulated nanoparticles could be harnessed to repair damage on the underlying surface. The simulations revealed that these capsules could deliver the encapsulated materials to specific sites on the substrate, thus effectively generating an alternate route to repairing surface defects. Once the healing nanoparticles had been deposited on the desired sites, the fluid-driven

capsules could move further along the surface, and for this reason the strategy was termed “repair-and-go.” The latter strategy might be particularly advantageous as it would have a negligible impact on the precision of the nondefective regions, and involve minimal amounts of the repair materials.

It is noteworthy that micron-sized capsules filled with dissolved particles can encompass very high payloads, allowing them very rapidly to carry and deliver large amounts of nanoparticles to a desired location. Furthermore, the continued, flow-driven motion of these micro-carriers, at least potentially, would allow multiple damaged regions to be healed by the capsules.

As the introduction of a synthetic microvasculature [15] into structural materials becomes more developed, the use of such microcapsules as cellular mimics could expand the efficiency of the artificial circulatory systems. In addition to supplying healing reagents in the channels, it could be advantageous to encapsulate “damage markers” within the microcapsules. The microcapsules would then continue to circulate in a “healthy,” undamaged system, but become trapped or localized at a damaged site and thus deliver a chemical “marker” (i.e., a visible or fluorescent dye) through its porous shell. Such markers would enable the nondestructive location and tracking of the damaged regions over time.

Below, attention is focused on describing the present authors’ studies with nanogels. In previous investigations [10], the lattice spring model (LSM) was utilized, which was adopted from atomistic models of solid-state and molecular physics [16]. The LSM involves a network of interconnected “springs,” which describe the interactions between neighboring units. The large-scale behavior of the resultant system can be mapped onto continuum elasticity theory [17]. Advantage was taken of the LSM to formulate new techniques for modeling the interactions between surface-functionalized, soft nanogels. Following Section 1.2, the findings on the behavior of dual crosslinked nanogel particles under strain are discussed, after which new calculations are described that allow modeling of the viscoelastic behavior of the individual nanogel particles.

1.2 Methodology

In this section, the computational approaches are described that were used to examine healing at the nanoscale. Specifically, we address the challenge of modeling deformable nanoscopic particles that are interconnected into a macroscopic network by both reactive and relatively nonreactive bonds. As noted above, the term “dual crosslinking” is used when referring to this material; here, the labile bonds allow the system to undergo significant structural rearrangement, while the strong “permanent” bonds provide an important “backbone.” It is the dynamic interplay between these different components that gives rise to the novel and distinctive characteristics of the materials.

A network of associated colloidal particles is commonly referred to a “particle gel.” To the best of the present authors’ knowledge, there have been no prior

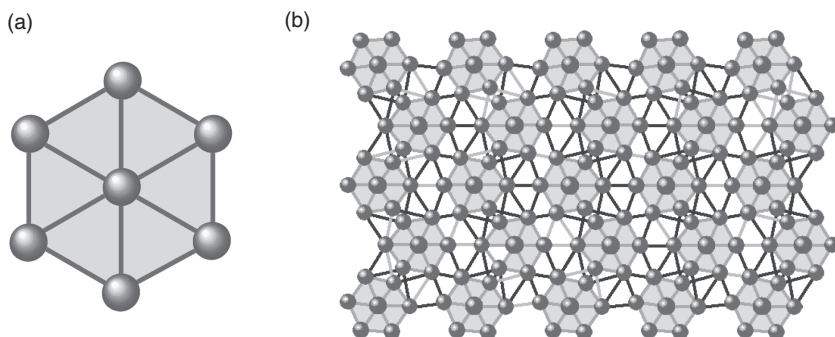


Figure 1.1 (a) Schematic of a deformable gel particle; each particle consists of seven nodes (points) connected by spring-like bonds (lines); (b) Fragment of an undeformed nanogel layer for sample with $P = 0.8$. The dark lines between units (shaded in gray) mark stable bonds, while light gray lines indicate labile bonds.

computational studies on particle gels where each individual particle is itself a deformable gel. Thus, these studies [10] represent the first simulations of a deformable network where each unit can itself undergo deformation.

The approach for simulating the nanogel network is based on the LSM [17, 18], where point-like masses (nodes) are interconnected by Hookean springs, which represent bonds. Figure 1.1a shows the seven-node model that represents the individual gel unit. These units are then interconnected into an extended material by both permanent and labile bonds.

Within a single gel unit, the nodes interact through a potential $U(r)$ that involves an attractive Hookean spring interaction, and a repulsive force, which mimics an excluded volume around the node:

$$U(r) = \frac{\kappa}{2} \left(r^2 + \frac{a}{r} \right) \quad (1.1)$$

with a cut-off distance r_c . Here, κ is the spring stiffness constant, r is the distance between the nodes, and a is the repulsion parameter. The equilibrium distance between the nodes is equal to $\Delta = (a/2)^{1/3}$. In the simulations, the cut-off distance r_c is set equal to 2Δ . Within each gel unit, the bonds do not break during the course of the simulations.

To model bonds between gel units, the same interaction potential is used, which emanates from each of the surface nodes on the gel pieces. Now, however, the spring constant κ for the inter-gel interactions is taken to be sixfold weaker than that for intra-gel bonds. (While different values for the latter spring constants could be chosen, it must be noted that for the large number of nodes considered here—in excess of 1000 for large samples—significant differences between the inter- and intra-gel spring constants can give rise to numerical instabilities.) Addi-

tionally, κ has the same value for stable and labile bonds. (The latter choice allowed attention to be focused specifically on isolating effects arising from the dual crosslinking.) In the case of a broken bond, the interaction potential is only given by the repulsive part (i.e., by the term $\propto 1/r$ in Equation 1.1).

The dynamical behavior of the system is taken to be in the overdamped limit, where the inertial terms in the equation of motion for the nodes is neglected. Thus, the velocity of a node is taken to be proportional to the net force acting on it (where the net force is the sum of forces from neighboring nodes and from an external tensile force). It must be noted that this assumption is commonly made in studies on gel dynamics [19, 20]. Specifically, each gel node obeys the following

dynamical equation: $\frac{d\mathbf{r}_i}{dt} = \mu\mathbf{F}_i$, where μ is the mobility and \mathbf{F}_i is the force acting on

node i . Here, μ is taken to be a constant, and thus the dependence of the mobility on the polymer density is neglected. The force acting on the node i is defined

as: $\mathbf{F}_i = -\frac{\partial U}{\partial \mathbf{r}_i} + \mathbf{F}_i^{\text{ext}}$, where the elastic energy U is equal to $U = \frac{1}{2} \sum_{m,n} 'U_i(|\mathbf{r}_m - \mathbf{r}_n|)$;

here, the prime denotes that the summation is for $m \neq n$. The term $\mathbf{F}_i^{\text{ext}}$ is the external force acting on particle i . In these simulations, $\mathbf{F}_i^{\text{ext}}$ is the tensile force applied to the nodes at the vertical edges of a rectangular sample. These equations of motion are then numerically integrated, using the fourth-order Runge–Kutta algorithm.

As explained above, in response to the applied deformation, the bonds between the gels units can rupture and reconnect. Thus, the Bell model [21] was adopted to describe the rupture and reformation of bonds. Recently, the Bell model has served as a useful framework for describing the relationship between bond dissociation and stress [22], and has also been widely used to describe the reversible bonds formed in proteins [23], between biological cells, or between cells and surfaces [24–26]. In accordance with the model [21, 25], the rupture rate, K_r , is an exponential function of the force applied to the bond:

$$K_r^{(s,l)} = \nu^{(s,l)} \exp\left[\frac{r_0 F - U_0^{(s,l)}}{k_B T}\right]. \quad (1.2)$$

Here, $U_0^{(s,l)}$ is the potential well depth at zero mechanical stress, F is the applied force, r_0 is a parameter that characterizes the change in the reactivity of the bond under stress, k_B is the Boltzmann constant, and T is the temperature. In the simulations, we set $r_0 = 0.2\Delta$, which is a representative value for chemical bonds [23]. The parameter $\nu^{(s,l)}$ is an intrinsic frequency of an unstressed bond; in the LSM, its value is equal to $\nu^{(s,l)} = \sqrt{\kappa/m}$, where κ is the bond stiffness and m is the reduced mass of the nodes attached to the bond (in the simulations, m was set to 1). The superscripts s and l label the stable and labile bonds, respectively. Taking representative values into consideration, the potential well depth was set equal to $U_0^{(l)} = 100k_B T$ for labile bonds, and to $U_0^{(s)} = 140k_B T$ for strong bonds [27].

The reforming rate, K_f , for a broken bond was calculated directly from the detailed balance principle [24, 26]:

$$\frac{K_r^{(s,l)}}{K_f^{(s,l)}} = \frac{K_{r0}^{(s,l)}}{K_{f0}^{(s,l)}} \exp\left(\frac{\Delta U^{(s,l)}}{k_B T}\right),$$

where $\Delta U^{(s,l)}$ is a difference in the potential energies of a connected and broken bond, and $K_{r0}^{(s,l)}$ and $K_{f0}^{(s,l)}$ are the rupture and reforming rates for an unstressed bond. For the Hookean spring interaction described by Equation 1.1, this gives [24, 26]:

$$K_f^{(s,l)} = K_{f0}^{(s,l)} \exp\left\{\kappa(r - \Delta)\left(r_0^{(s,l)} - (r - \Delta)/2\right)(k_B T)^{-1}\right\} \quad (1.3)$$

The probability for a connected bond to break and the probability for a broken bond to reform within a numerical time step Δt were taken to be of the following forms:

$$\begin{aligned} w_r^{(s,l)} &= 1 - \exp[-K_r^{(l,s)} \Delta t], \\ w_f^{(s,l)} &= 1 - \exp[-K_f^{(l,s)} \Delta t]. \end{aligned} \quad (1.4)$$

At each simulation time step, the probability of bond rupturing or reforming is computed according to Equation 1.4, where $\Delta t = 10^{-2}$ is the time step of integration.

Gel samples of three different sizes were considered: (i) five rows, with 10 particles in each row; (ii) 10 rows with 10 particles in each row; and (iii) 12 rows with 15 particles in each row. To prepare dual crosslinked materials with different distributions of labile and permanent bonds, these samples were constructed in two steps. In the first step, the layers were arranged into a regular pattern with a lattice spacing of 3Δ between the centers of the gel units, where Δ is the equilibrium distance between the nodes (2Δ is the horizontal size of a gel unit). The vertical spacing between the layers was equal to 1.3Δ . At this step, all possible bonds within the cut-off radius were established, and each node was allowed to subtend at most five interactions. All of these interactions were marked as labile bonds. The sample was then equilibrated for 100 time steps (for the smallest sample), or 1000 time steps (for larger samples). During the equilibration, the initial mechanical stresses undergo relaxation, and the most stressed bonds were ruptured in accordance with the probability in Equation 1.4. In the second step, the characteristics of each interparticle bond were specified, assigning stable bonds with a probability P and labile bonds with a probability $(1 - P)$. Thus, even for a fixed value of P , each simulation has a different, independent distribution of stable and labile bonds.

1.3

Towards Self-Healing Organic Nanogels

1.3.1

Response of Samples to Tensile Deformation

In the simulations, the interconnected gel particles form a two-dimensional (2-D) network (see Figure 1.1b). Given that N_{sta} and N_{lab} are the respective average

number of stable and labile bonds in the system, the ratio $P = N_{sta} / (N_{sta} + N_{lab})$ is used to characterize the interconnections in the network. For example, for $P = 1$, the nanogel particles are interconnected solely by the stable bonds, whereas for $P = 0.8$, the material encompasses 20% labile bonds. In this case, P is referred to as the dual crosslinking ratio.

Below are described the findings for larger samples; namely, those that encompassed eight rows of gel particles, with 10 particles in each row, and a sample with 12 rows, where each row consisted of 15 particles. In order to characterize the behavior of the system, a Weibull statistical analysis [28] was carried out on these samples. In the relatively thin samples, a certain fraction of the labile bonds are located in the outer surface of the film. When the tensile deformation was applied [10], some of these bonds were readily broken (as they had fewer neighbors to bind them), and this process effectively nucleated a small surface crack which then initiated the ensuing dynamic processes. As the width of the sample was increased, however, the relative fraction of surface bonds decreased. To ensure that the simulations are run in realistic time scales, for the larger samples, a small notch was initially introduced at a random site at the surface, after which the analysis was carried out, as described below.

Following the introduction of a crack at the lower surface (as shown by the vertical arrows in Figure 1.2), the sample was stretched by a tensile force. It was then determined whether the sample fractured after being stretched at a given stress, σ , or not. The simulation was repeated eight times, with different initial positions for the crack. The probability of rupture, p_b , was calculated as a ratio of the number

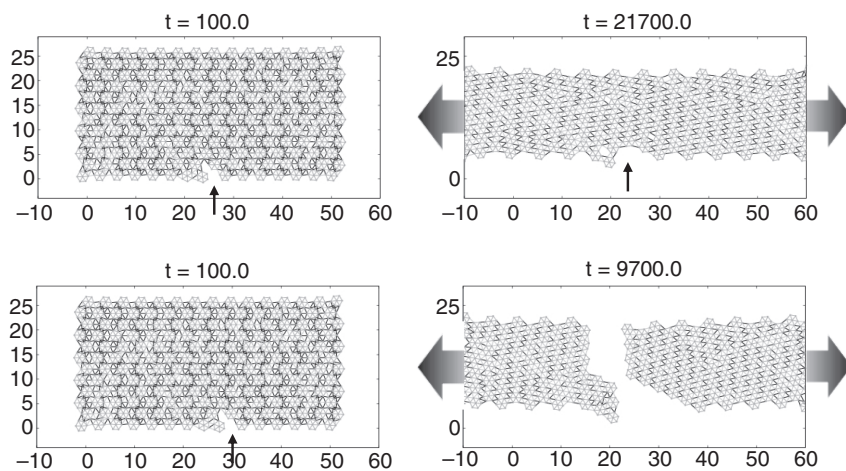


Figure 1.2 Two different realizations of a large sample, which is composed of 12 rows of gel clusters, with 15 clusters in a row. The dual crosslinking ratio is $P = 0.8$. The initial cracks are marked by vertical arrows. Large horizontal arrows indicate the direction of the stretching forces that are applied to the sample's edges. Top row: The sample is stable for 2100 time steps before a structural rearrangement takes place. Bottom row: the sample fractures at $t \sim 9700$ numerical time steps. It is clearly seen that fracture is initiated at the crack.

of times that the sample was completely fractured, n_b , compared to the total number of attempts, n_{tot} ($p_b = n_b / n_{tot}$).

In the Weibull statistical analyses, the probability of a sample breaking is described by the two-parameter cumulative distribution function:

$$p_b(\sigma) = 1 - \exp\left[-(\sigma/\sigma_b)^m\right], \quad (1.5)$$

where σ_b and m are the fitting parameters characterizing the distribution. The parameter σ_b is the characteristic stress at which the sample fractures, and the exponent m characterizes the brittleness of the sample.

The results of the analysis for the two larger samples are quantitatively similar; thus, the data for the largest sample are presented in Figure 1.3. The plot in Figure 1.3a shows the dependence of the probability of rupture, p_b , on the applied stress σ for a sample with $P = 0.8$; each point represents an average of eight independent simulations. The stress σ is normalized by the stiffness of the bond, κ (see Section 1.2), which has the same dimensionality as σ in two dimensions (so that the ratio σ/κ is dimensionless). The curve shows the result of fitting the numerical data to the function $p_b(\sigma)$ in Equation 1.5. The fitting parameters were determined with the aid of the least-squares method. The values for the relevant parameters were $\sigma_b/\kappa = 0.83 (\pm 0.04)$ and $m = 5.15 (\pm 0.04)$ for $P = 0.8$. Thus, the statistical error in the determination of the fitting parameters was $\sim 5\%$ for the characteristic rupture stress σ_b , and less than 1% for the exponent m . It can be seen that, for $P = 0.8$, the curve characterizing p_b exhibits a gentle slope.

By generating plots similar to Figure 1.3a for different values of P , the curve in Figure 1.3b is obtained, which shows the dependence of the characteristic rupture stress σ_b on the dual crosslinking ratio P . The error bars in this plot show the standard deviations for σ_b obtained via the fitting procedure. The maximum in the plot at $P \sim 0.7$ clearly shows that the stress needed to fracture a material with a small fraction of reactive bonds is greater than that required to fracture a material composed entirely of the stable bonds.

1.3.2

Stress–Strain Curve

In order to more completely characterize the behavior of this dual-crosslinked material under tensile deformation, and to demonstrate its self-healing properties, the stress–strain curves were also determined. In contrast to the simulations described above, where a constant stress was applied to a sample, in this case the sample was stretched at a constant velocity, and the tensile stress was computed as a function of the strain, $\varepsilon = (L - L_0)/L_0$. (In particular, the right edge of the sample was held fixed, while the left edge was displaced along the horizontal axes with a speed V_x .) This type of measurement is widely used in the characterization of crosslinked polymers [29, 30]. It should be noted that the engineering stress [31], which is defined as the ratio of the tensile force to the cross-section (in the Y direction) of the unperturbed layer, is calculated. At regions of high strain, where

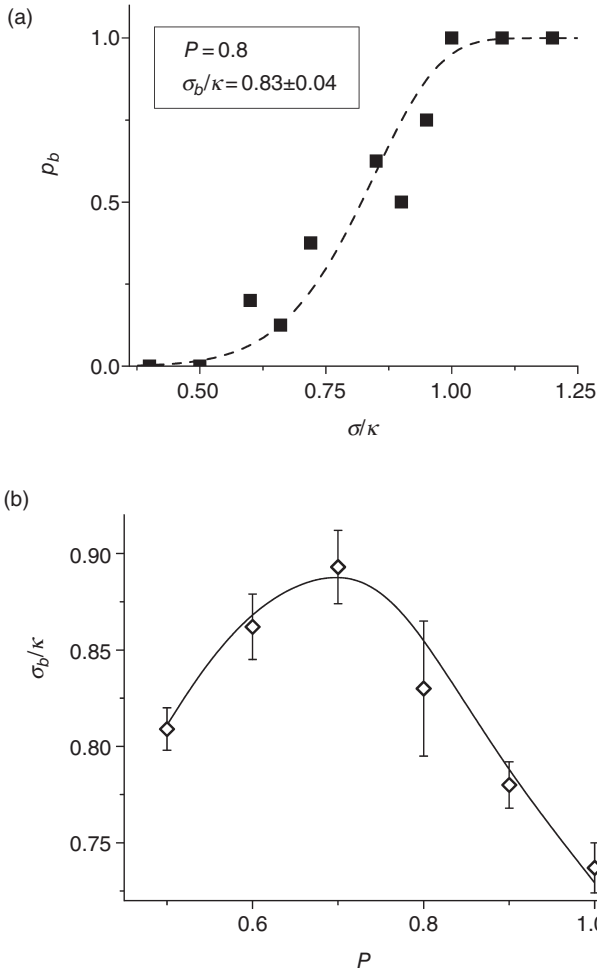


Figure 1.3 (a) Probability for the sample to break, p_b , plotted as a function of the applied tensile stress, σ . The solid squares show the results from simulations for dual crosslinked samples with $P = 0.8$. The dashed curve shows the results of fitting of the data by the Weibull probability distribution function. The

stress is normalized by the bond stiffness constant, κ ; (b) The diamonds show the dependence of σ_b on the dual crosslinking ratio P , as calculated through Weibull statistical analyses for the largest sample. The full curve is plotted as a guide for the eye.

structural rearrangement takes place, the true stress is higher than the calculated engineering stress, due to the decrease in the sample's cross-section during the course of the rearrangement. Thus, these calculations provide an estimate from below for the stability region of materials encompassing labile bonds ($P < 1$).

Figure 1.4 shows the stress–strain curves calculated for the largest sample (with 12 rows with 15 particles in each row) for $P = 1$ and $P = 0.8$. Here, the tensile

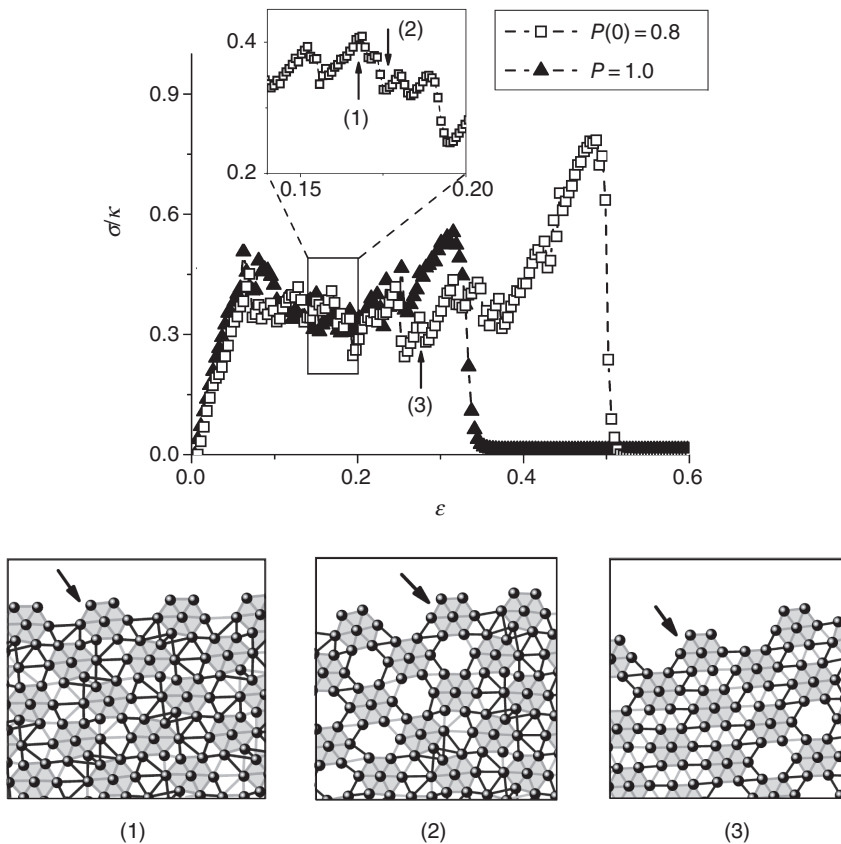


Figure 1.4 Upper diagram: Stress–strain curve calculated for the largest sample. Stress is normalized by the bond stiffness constant, κ . The open squares mark the results for dual crosslinked samples $P(0) = 0.8$; filled triangles indicate the results for the permanently crosslinked $P = 1$ samples. The dashed curves are plotted to guide the eye. The inset shows jumps in the stress–strain curve on an enlarged scale. Lower diagrams: Panels (1–3) showing the evolution of a portion of the sample with increasing strain, ϵ . The moments in time at which the panels are plotted are labeled in the upper plot by vertical arrows. Panels (1) and (2) show the respective images of the sample just before and after the formation of holes between the gel particles because of the bond rupture. Panel (3) shows the same sample after the holes have collapsed, at a later time. A cluster positioned near these structural rearrangements is marked by slanted arrow.

speed was equal to $V_i = 10^{-3} d/\tau$, where $d = 2\Delta$ is the characteristic size of the gel particle. The parameter $\tau = 1/\mu\kappa$ is the elastic response time for a bond, where μ is the mobility of the nodes and κ is the stiffness of the bonds (see below and Section 1.2). The first peak at $\epsilon \approx 0.08$ provides the yield stress, while at stresses below the yield stress the curves for the permanent and dual crosslinked samples coincide with each other. The latter behavior arises because the stiffness constants for the strong and labile bonds are chosen to be equal. The lower panels (1–3) in Figure 1.4 illustrate the mechanism of structural rearrangement (plastic elonga-

tion) of the sample for $\varepsilon > 0.08$. As is apparent from panels (1) and (2), elongation of the sample at $\varepsilon > 0.08$ is accompanied by rupture of bonds and the formation of cavities in the sample bulk. (The formation of cavities during the plastic deformation of solid samples was also observed in molecular dynamics simulations in crosslinked polymers [29, 30, 32].) The bond rupture is also responsible for the saw-tooth-shaped fluctuations seen in the stress–strain curves, and is clearly visible in the inset. In the case of the dual crosslinked sample, the cavities collapse at later times due to the formation of new labile bonds between the clusters, as is evident from panel (3) (see also Figure 1.2). In effect, the dual crosslinking allows the particles to move relative to each other, without compromising the structural integrity of the sample and thereby, to decrease the strain energy.

It is clear from Figure 1.4 that the strain at which the $P = 0.8$ dual crosslinked sample fractures ($\varepsilon_b \approx 0.5$) is approximately 1.5-fold greater than that for the sample with $P = 1.0$ ($\varepsilon_b \approx 0.33$). Furthermore, the stress needed to fracture the $P = 0.8$ sample is greater than σ^* , which is the stress necessary to fracture the $P = 1$ material. The latter finding is in agreement with the plot in Figure 1.3, which was obtained from simulations involving constant applied stress. These observations support the conclusion that the introduction of labile bonds leads to an increase in the mechanical stability of the nanogel material.

Figure 1.5a reveals how the total number of bonds in the sample, $N_{tot} = N_{lab} + N_{sta}$, vary with the applied strain for the tensile deformation shown in Figure 1.4. The data are plotted up to the point where the samples undergo fracture: $\varepsilon \approx 0.5$ for $P = 0.8$ and $\varepsilon \approx 0.33$ for $P = 1.0$. While the total number of bonds is decreased during the deformation for both $P = 0.8$ and $P = 1.0$ samples, the total number of bonds for the dual crosslinked sample is always higher than that for the permanently crosslinked sample in the plastic deformation region $\varepsilon > 0.08$. This difference is due to the reformation of ruptured labile bonds during the structural rearrangement.

To further characterize changes in the network during rearrangement in the dual crosslinked sample, the saturation parameter $s = N_{lab} / N_{lab}^{(max)}$ is defined; this is the ratio of the number of formed labile bonds to the maximally permitted number of labile bonds in the sample. The total number of labile bonds is limited in the model by the total number of nodes on the surface of the gel particles (see Section 1.2). The dependence of s on ε for the $P = 0.8$ sample is plotted in the inset in Figure 1.5b. Initially, only approximately 28% of all possible labile bonds were formed in the sample; all the other labile bonds were sufficiently stressed that they ruptured, in accordance with the probability in Equation 1.2. During rearrangement of the sample, the number of labile bonds was gradually increased, and reached $s \approx 0.5$ before the sample fractured.

On the other hand, the less-reactive, stable bonds mostly simply rupture (without reforming) during rearrangement for the $P = 1$ sample (see Figure 1.5a). As a consequence, the value of P (the ratio of the number of stable bonds to the total number of bonds) is decreased from its initial value of $P = 0.8$ to $P \approx 0.53$ during the course of deformation (as shown in Figure 1.5b). These data support the contention that reforming of the labile bonds plays a crucial role in maintaining the stability of dual crosslinked samples.

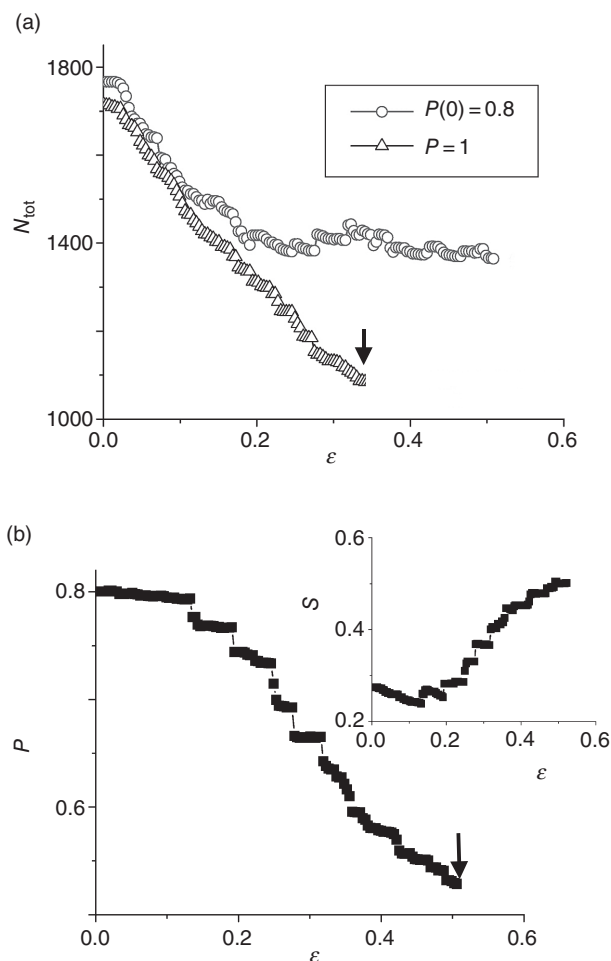


Figure 1.5 (a) Changes in the total number of bonds in the sample at the initial crosslinking ratio $P(0) = 0.8$ (circles) and at $P = 1.0$ (triangles) during the deformation shown in Figure 1.4; (b) Dependence of P on strain ϵ , calculated for the same simulation. Inset: Saturation s in the labile bond network as a function of strain. The vertical arrows in (a) and (b) mark the strain at which the sample fractured.

1.3.3

Tensile Strength of Nanogel Samples

Finally, an investigation was made into how the stability of the samples depends on V_b , the rate of the tensile deformation. Calculations were performed for rates V_t in the range from 10^{-4} through $10^{-2} \times d/\tau$. At any given rate, a stress–strain curve similar to that shown in Figure 1.4 was calculated for the largest sample with

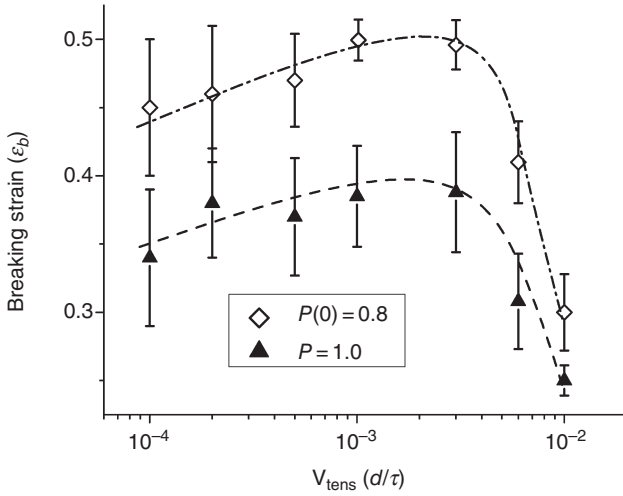


Figure 1.6 Dependence of σ_b on tensile rate, shown on a logarithmic scale for the largest sample at $P(0) = 0.8$ (diamonds) and $P = 1.0$ (triangles).

a randomly placed crack on its surface. The strain at which the sample fractured into two pieces, ϵ_b , was determined in each simulation as the strain at which the stress–strain curve dropped sharply to zero. The results obtained for ϵ_b were averaged over eight independent simulations made with different positions of the crack. The results for the $P = 0.8$ and $P = 1.0$ samples are summarized in Figure 1.6, where the points show the averaged values for ϵ_b and the error bars mark the standard deviations. The plots reveal a maximum at a tensile rate of $V_t \sim 2 \times 10^{-3} \times d/\tau$ for both dual and permanently crosslinked samples. Note that a maximum in the dependence of ϵ_b on the tensile rate is known to occur for permanently crosslinked elastomers in the regime where viscoelastic effects are important [33]. It is also evident from Figure 1.6 that, at any tensile rate, the ϵ_b calculated for the $P = 0.8$ sample was from ~20% (at the fastest tensile rates $V_t \geq 6 \times 10^{-3} \times d/\tau$) to 30% (at slower tensile rates, $V_t < 6 \times 10^{-3} \times d/\tau$) higher than that for the $P = 1.0$ sample. This was in accordance with the results described above for the calculations at constant velocity. Of note, it follows from Figure 1.6 that the stress–strain curves shown in Figure 1.4 were computed for conditions near the maximum of the $\epsilon_b(V_t)$ dependence.

1.3.4

Modeling Viscoelastic Nanogel Particles

In Section 1.3.3, the individual nanogel particles were modeled as purely elastic objects, and the relaxation processes within the system were due solely to the rearrangement of bonds interconnecting the nanogels. In order to capture viscoelastic behavior, the gel lattice spring model (gLSM) [34] was introduced into the

computational framework, so as to allow a generalization of the methodology to a broader range of materials. To formulate this gLSM, we first determined the energy density within the deformed material through the use of a phenomenological model of viscoelasticity. A finite element approximation was then employed to describe the deformation field in terms of a set of nodal coordinates. Finally, Newton's second law was used to derive the equations of motion for the nodal points. Each of these steps is described below.

First, an isotropic solid body that undergoes a time-dependent deformation $\mathbf{X} \rightarrow \mathbf{x}(\mathbf{X}, t)$ is considered. Here, \mathbf{X} represents the coordinates of a point within the material in the initial, undeformed state, whereas \mathbf{x} is the position of the same point upon deformation at time t . The local strain is characterized by the Finger tensor [35] $\hat{\mathbf{B}}(t) = \hat{\mathbf{F}}(t) \cdot \hat{\mathbf{F}}^T(t)$, where

$$[\hat{\mathbf{F}}(t)]_{ij} = \frac{\partial x_i(\mathbf{X}, t)}{\partial X_j}, \quad i, j = 1, 2, 3, \quad (1.6)$$

is the deformation-gradient tensor, and the superscript "T" represents the transposition operation. In purely elastic solids, the local stresses at a time t depend on the local strains at the same time t ; that is, the elastic stress tensor $\hat{\boldsymbol{\sigma}}_{\text{el}}(t)$ is a function of the strain tensor $\hat{\mathbf{B}}(t)$. If, however, the solid is viscoelastic, then the local stresses depend on the deformation history. Hence, the stress tensor $\hat{\boldsymbol{\sigma}}^*(t)$ is a *functional* of the relative strain tensor $\hat{\mathbf{b}}(t, t')$, which characterizes deformations in the body at time t relative to the state of the body at $t' \leq t$ [36]. The relative strain tensor can be determined through the following decomposition:

$$\hat{\mathbf{b}}(t, t') = \hat{\mathbf{F}}(t) \cdot \hat{\mathbf{C}}^{-1}(t') \cdot \hat{\mathbf{F}}^T(t), \quad (1.7)$$

where $\hat{\mathbf{C}}(t) = \hat{\mathbf{F}}^T(t) \cdot \hat{\mathbf{F}}(t)$ is the left Cauchy–Green strain tensor; $\hat{\mathbf{b}}(t, 0) = \hat{\mathbf{B}}(t)$, since the body is assumed to be undeformed at $t' = 0$.

The constitutive equation (i.e., the stress–strain relationship) can be determined if the energy dependence on the strain is known. It is assumed that the strain energy density, U , which is defined per unit volume of unstrained material, is represented as a sum of two contributions: $U = U_{\text{el}} + U^*$, where U_{el} describes the purely elastic deformations and U^* is the viscoelastic contribution to the strain energy. Correspondingly, the stress tensor also consists of the two contributions: $\hat{\boldsymbol{\sigma}}(t) = \hat{\boldsymbol{\sigma}}_{\text{el}}(t) + \hat{\boldsymbol{\sigma}}^*(t)$. The dependence of the stress tensors $\hat{\boldsymbol{\sigma}}_{\text{el}}(t)$ and $\hat{\boldsymbol{\sigma}}^*(t)$ on the respective strain tensors $\hat{\mathbf{B}}(t)$ and $\hat{\mathbf{b}}(t, t')$ is determined by the choice of U_{el} and U^* .

The elastic energy density U_{el} depends only on $\hat{\mathbf{B}}$ through the invariants of this tensor I_i , $i = 1, 2, 3$, that is, $U_{\text{el}} = U_{\text{el}}(I_1, I_2, I_3)$ [35]. The invariants are calculated as follows:

$$I_1 = \text{tr} \hat{\mathbf{B}}, \quad I_2 = \frac{1}{2}[(\text{tr} \hat{\mathbf{B}})^2 - \text{tr}(\hat{\mathbf{B}}^2)], \quad I_3 = \det \hat{\mathbf{B}}. \quad (1.8)$$

It is worth noting that $I_3^{1/2} = dV / dV_0$ is the relative volumetric change in a material element due to the deformation, where dV and dV_0 are the element volumes in

the deformed and undeformed states, respectively. Below, the notation $J = I_3^{1/2}$ will also be used. The constitutive equation for the purely elastic stress can be written in the following general form: [35]

$$\hat{\boldsymbol{\sigma}}_{\text{el}} = 2I_3^{-1/2}(w_2I_2 + w_3I_3)\hat{\mathbf{I}} + 2I_3^{-1/2}w_1\hat{\mathbf{B}} - 2I_3^{1/2}w_2\hat{\mathbf{B}}^{-1}, \quad (1.9)$$

where $\hat{\mathbf{I}}$ is a unit tensor and

$$w_i = \frac{\partial}{\partial I_i} U_{\text{el}}(I_1, I_2, I_3), \quad i = 1, 2, 3. \quad (1.10)$$

To specify the elastic contribution to the strain energy of the nanogels, the so-called “neo-Hookean compressible material” model is employed [36, 37]. Within this model, the elastic strain energy depends only on I_1 and I_3 , and has the following form:

$$U_{\text{el}} = 1/2c_0(I_1 - 3) + 1/2K \log^2(J). \quad (1.11)$$

The first term on the right-hand-side of Equation 1.11 depends only on I_1 , and describes the contribution from the shear deformations. The second term on the right-hand-side of Equation 1.11 is the energy of bulk deformations, that is a function of the volumetric change J . The c_0 and K are the model parameters, which are proportional to the shear and bulk moduli, respectively. Note that $K \gg c_0$, since the bulk modulus is usually much greater than the shear modulus. The substitution of Equation 1.11 into Equation 1.9 results in the following equation for the purely elastic stress contribution:

$$\hat{\boldsymbol{\sigma}}_{\text{el}}(t) = c_0 J^{-1}(t) \hat{\mathbf{B}}(t) + K J^{-1}(t) \log[J(t)] \hat{\mathbf{I}} \quad (1.12)$$

The general form of the viscoelastic contribution to the energy density U^* also depends only on the invariants $I_i(t, t')$, $i = 1, 2, 3$, of the relative stress tensor $\hat{\mathbf{b}}(t, t')$. In polymeric materials, the shear deformations exhibit strong relaxation effects, whereas the bulk deformations are essentially purely elastic. Therefore, it can be assumed that U^* only includes the contribution from the relaxing shear stresses. The latter contribution can be generalized from the elastic neo-Hookean term in Equation 1.11 (the first term that depends on $I_1(t)$) to the case of viscoelastic behavior, so that U^* depends on the first invariant $I_1(t, t')$ of the relative strain tensor. The following simple generalization of the neo-Hookean term is utilized [36]:

$$U^* = 1/2\chi(t, 0)[I_1(t, 0) - 3] + 1/2 \int_0^t \frac{\partial \chi}{\partial t'}(t, t')[I_1(t, t') - 3] dt'. \quad (1.13)$$

Here, $\chi(t, t')$ gives the viscoelastic strain energy generated at time t' that remains unrelaxed at time $t \geq t'$. The corresponding constitutive equation for the viscoelastic stress is [36]:

$$\hat{\boldsymbol{\sigma}}^*(t) = \chi(t,0)J^{-1}(t)\hat{\mathbf{b}}(t,0) + J^{-1}(t)\int_0^t \frac{\partial \chi}{\partial t'}(t,t')\hat{\mathbf{b}}(t,t')dt'. \quad (1.14)$$

The viscoelastic behavior of the nanogels is modeled by assuming a simple exponential relaxation:

$$\chi(t,t') = c_0^* \exp[-(t-t')/\tau_R], \quad (1.15)$$

where c_0^* contributes to the unrelaxed shear modulus and τ_R is the relaxation time.

After the stress–strain relationships (Equations 1.12 and 1.14) have been specified, the dynamics of each nanogel particle is described by the following continuum equation:

$$\rho[\partial_t \mathbf{v} + (\mathbf{v} \cdot \nabla)\mathbf{v}] = \nabla \cdot (\boldsymbol{\sigma}_{el} + \boldsymbol{\sigma}^*). \quad (1.16)$$

Here, ρ is the mass density, which depends on the volumetric changes J , and $\rho = \rho_0 J^{-1}$, where ρ_0 is the nanogel density in the undeformed state. For each nanogel particle, Equation 1.16 is subject to boundary conditions due to the inter-particle interactions.

The numerical integration of Equation 1.16 can be readily performed using the gLSM; this entails approximating a nanogel particle by a number of finite elements and solving the equations of motion for the nodal points of the elements. The gLSM approach is illustrated by considering the 2-D nanogel particle shown in Figure 1.7a. The nanogel is modeled as a three-dimensional (3-D) particle confined in a slit of thickness $H = \lambda_{\perp} H_0$, where H_0 is the particle height in the undeformed state, and λ_{\perp} is the uniform compressive strain imposed on the particle in the direction perpendicular to the slit surface. It is assumed that motion of the particle along the slit surface is frictionless, so that the particle dynamics can be considered as purely 2-D.

The shape of the hexagonal nanogel particle shown in Figure 1.7a is best captured by six equal triangular finite elements, each of which is labeled by the integer number $m = 1, 2, \dots, 6$ (see Figure 1.7a). The nodes within the element m are labeled by $n = 1, 2, 3$ in the counter-clockwise direction (see Figure 1.7b). The position of a node is given by $\mathbf{x}_n(m)$. In the undeformed state, the elements are assumed to have a uniform density ρ_0 , and the elemental area is A_0 . In the finite element approximation, the total energy of a system is equal to the sum of the energies of the elements; that is, $W = \int U dV_0 \approx H_0 A_0 \sum_m U(m)$, and each elemental energy $U(m)$ is expressed in terms of the nodal coordinates. The force acting on the node n belonging to the element m is obtained by differentiating W with respect to $\mathbf{x}_n(m)$. The elemental contribution to the equation of motion is then written as:

$$1/3\rho_0 \frac{d^2}{dt^2} \mathbf{x}_n(m) = -\frac{\partial U(m)}{\partial \mathbf{x}_n(m)}. \quad (1.17)$$

If a node is common to several adjacent elements, then the equation of motion for the node is obtained by summation of the elemental contributions given by Equation 1.17.

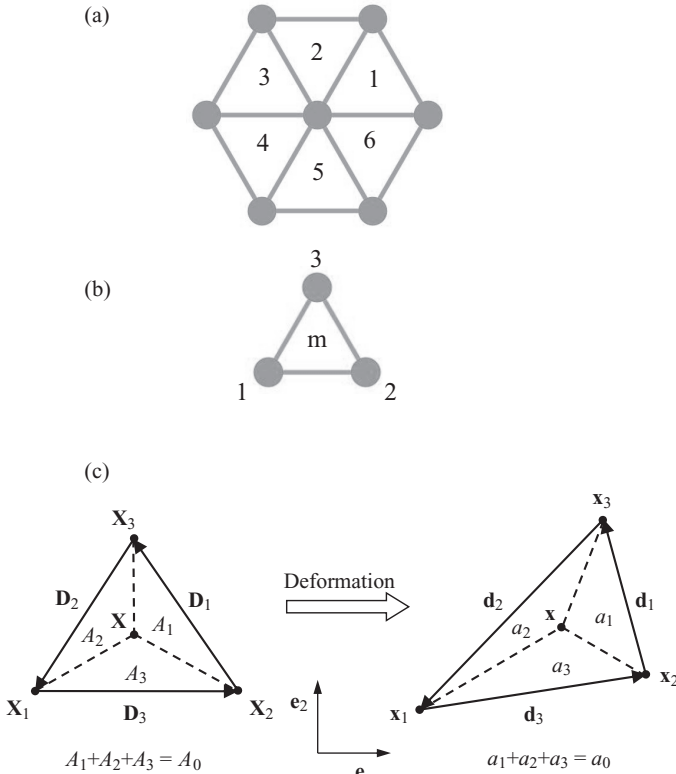


Figure 1.7 (a) Schematic of a viscoelastic nanogel cluster approximated by six triangular elements. Each element is labeled by an integer number $m = 1, 2, \dots, 6$; (b) Notation for the node labeling in an m th viscoelastic triangular element. The nodes within the element are labeled as 1, 2, or 3, where the node shared by all elements in the center of the cluster is marked as 1, and the rest of the

nodes are marked sequentially in a counterclockwise direction; (c) Triangular element in undeformed (left) and deformed (right) states. \mathbf{X} is an arbitrary point within the unit. The vectors $\mathbf{e}_1, \mathbf{e}_2$ define the 2-D reference frame used in the simulations. A_i and a_i are the areas of the triangles (as shown in the figure), and A_0 and a_0 are the total area of the unit before and after deformation.

First, let us consider the triangular element m in the hexagonal gel (below, the element label is omitted for brevity). As indicated in Figure 1.7c, the element nodes have the coordinates \mathbf{X}_n , $n = 1, 2, 3$ in the undeformed state. The edge vectors \mathbf{D}_n , $n = 1, 2, 3$, are also introduced, where

$$\mathbf{D}_1 = \mathbf{X}_3 - \mathbf{X}_2, \mathbf{D}_2 = \mathbf{X}_1 - \mathbf{X}_3, \mathbf{D}_3 = \mathbf{X}_2 - \mathbf{X}_1, \quad (1.18)$$

so that the edge n is located opposite to the node n (see Figure 1.7c). Note that $\sum_n \mathbf{D}_n = 0$. Any point \mathbf{X} within the triangle can be uniquely parameterized using the local triangular coordinates L_n [38]:

$$\mathbf{X} = \sum_{n=1}^3 L_n \mathbf{X}_n, \quad (1.19)$$

The values of L_n , which are also known as the shape functions, are defined as $L_n = A_n / A_0$, where A_n is the area of the triangle formed by the point \mathbf{X} and the end points of the edge n , and $\sum_n A_n = A_0$ is the total area of the undeformed triangle. The value of A_n can be determined through the coordinates of the point \mathbf{X} and the nodal coordinates as:

$$A_n = 1/2 \|\mathbf{D}_n \times (\mathbf{X} - \mathbf{X}_{n-1})\|. \quad (1.20)$$

The above definitions are illustrated in Figure 1.7c.

Displacement of the nodal points $\mathbf{X}_n \rightarrow \mathbf{x}_n(t)$ results in deformation of the interior of the element, and the areas A_n also change, $A_n \rightarrow a_n$ (as illustrated in Figure 1.7c). The total area of the deformed triangle is $a_0 = \sum_n a_n$. The deformation $\mathbf{X} \rightarrow \mathbf{x}(\mathbf{X})$ is then approximated by linear functions of \mathbf{X} . In this case, $a_n / a_0 = A_n / A_0 = L_n$, so the position of the point $\mathbf{x}(\mathbf{X})$ in the deformed triangle is characterized by the same triangular coordinates L_n as for the point \mathbf{X} of the undeformed element (Figure 1.7c):

$$\mathbf{x}(\mathbf{X}, t) = \sum_{n=1}^3 L_n(\mathbf{X}) \mathbf{x}_n(t). \quad (1.21)$$

The above equation indicates explicitly that $L_n = L_n(\mathbf{X})$, according to Equation 1.20.

By using Equation 1.21 to approximate the deformation field within a triangular element, it is possible to determine the element strain–energy density U as a function of the nodal points. To facilitate this computation, the base vectors \mathbf{g}_i are introduced as

$$\mathbf{g}_i = \frac{\partial \mathbf{x}}{\partial X_i}, \quad i = 1, 2, 3, \quad (1.22)$$

and the matrix element for the left Cauchy–Green tensor is given in terms of \mathbf{g}_i as

$$[\mathbf{C}(t)]_{ij} = \mathbf{g}_i(t) \cdot \mathbf{g}_j(t) \quad \text{and} \quad [\mathbf{C}^{-1}(t)]_{ij} = \varepsilon_{ikl} \varepsilon_{jmn} \frac{(\mathbf{g}_k \times \mathbf{g}_l) \cdot (\mathbf{g}_m \times \mathbf{g}_n)}{[\mathbf{g}_1 \cdot (\mathbf{g}_2 \times \mathbf{g}_3)]^2}, \quad (1.23)$$

where ε_{ijk} is the Levi–Civita tensor. According to Equations 1.21 and 1.22, the base vectors depend on the nodal coordinates as

$$\mathbf{g}_i(t) = \sum_{n=1}^3 \frac{\partial L_n}{\partial X_i} \mathbf{x}_n(t). \quad (1.24)$$

The time dependence of the base vectors can be expressed in terms of the instantaneous values of the edge vectors \mathbf{d}_n as

$$\begin{aligned} \mathbf{g}_1(t) &= \frac{1}{2A_0} [(\mathbf{D}_2 \cdot \mathbf{e}_2) \mathbf{d}_1(t) - (\mathbf{D}_1 \cdot \mathbf{e}_2) \mathbf{d}_2(t)], \\ \mathbf{g}_2(t) &= -\frac{1}{2A_0} [(\mathbf{D}_2 \cdot \mathbf{e}_1) \mathbf{d}_1(t) - (\mathbf{D}_1 \cdot \mathbf{e}_1) \mathbf{d}_2(t)], \end{aligned} \quad (1.25)$$

$$\mathbf{g}_3(t) = \lambda_{\perp} \mathbf{e}_3,$$

where $\mathbf{d}_n(t) = \mathbf{x}_{n+2}(t) - \mathbf{x}_{n+1}(t)$ and \mathbf{D}_n are defined by Equation 1.18. The invariants of the strain tensors are calculated by substituting Equation 1.25 into Equation 1.23 to obtain

$$I_1(t) \equiv \mathbf{g}_1^2 + \mathbf{g}_2^2 + \mathbf{g}_3^2 = \sum_{n,m} \Gamma_{nm}^{(0)} \mathbf{x}_n(t) \cdot \mathbf{x}_m(t), \quad (1.26)$$

$$I_1(t, t') \equiv \text{tr}[\mathbf{C}(t) \cdot \mathbf{C}^{-1}(t')] = \sum_{n,m} \Gamma_{nm}(t') \mathbf{x}_n(t) \cdot \mathbf{x}_m(t). \quad (1.27)$$

The matrix elements $\Gamma_{nm}^{(0)}$ depend on the element shape in the equilibrium state, whereas the values $\Gamma_{nm}(t')$ retain information concerning the deformation history, namely:

$$\Gamma_{nm}^{(0)} = \frac{\mathbf{D}_n \cdot \mathbf{D}_m}{(2A_0)^2}, \quad \Gamma_{nm}(t) = \frac{\mathbf{d}_n(t) \cdot \mathbf{d}_m(t)}{[\mathbf{d}_n(t) \times \mathbf{d}_m(t)]^2}. \quad (1.28)$$

Similarly, the relative volume ratio between the deformed and undeformed gel, J , can be calculated as

$$J(t) \equiv \mathbf{g}_1(t) \cdot [\mathbf{g}_2(t) \times \mathbf{g}_3(t)] = \lambda_{\perp} (2A_0)^{-1} \mathbf{e}_3 \cdot [\mathbf{d}_1(t) \times \mathbf{d}_2(t)]. \quad (1.29)$$

The substitution of Equations 1.26, 1.27 and 1.29 into Equations 1.11, 1.13 and 1.16 yields the elemental energy density as a function of the nodal coordinates:

$$U(t) = c_0 \sum_{nm} \Gamma_{nm}^{(0)} (\mathbf{x}_n(t) \cdot \mathbf{x}_m(t)) + 1/2K \log^2[\lambda_{\perp} (2A_0)^{-1} \mathbf{e}_3 \cdot (\mathbf{d}_1(t) \times \mathbf{d}_2(t))] + c^* \sum_{nm} \theta_{nm}(t) (\mathbf{x}_n(t) \cdot \mathbf{x}_m(t)) \quad (1.30)$$

Here, the dimensionless functions $\theta_{nm}(t)$ describe the relaxation processes and are obtained by solving the following rate equations:

$$\tau_R \frac{d\theta_{mn}(t)}{dt} = -\theta_{mn}(t) + \Gamma_{mn}(t), \quad (1.31)$$

where τ_R is the relaxation time, and $\Gamma_{mn}(t)$ is determined by Equation 1.28. Equation 1.31 was obtained by differentiating Equation 1.13, with Equation 1.15 taken into account. Finally, the force on the node n of the element m is calculated according to Equation 1.17.

It can now be demonstrated that the formulation developed above captures the creep and stress relaxation behavior that is characteristic of viscoelastic solids. Below are presented the results of computer simulations performed for the triangular finite element and the entire hexagonal nanogel particle. The dynamic equations were transformed to the dimensionless form using the length and time scales of $L_0 = \Delta$ and $T_0 = (\rho_0 \Delta^2 / c_0)^{1/2}$, respectively, where Δ is the lateral size of the

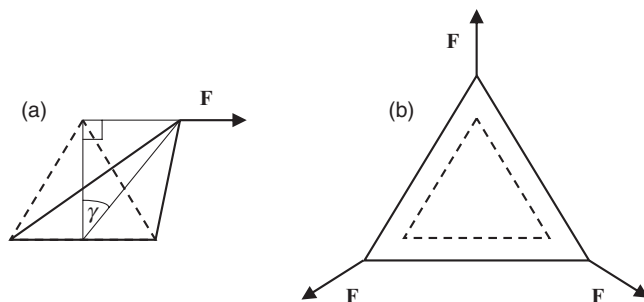


Figure 1.8 Scheme depicting (a) shear and (b) bulk modes of deformation of a triangular element shown in Figure 1.7b. The equilibrium shape of the element is shown by the dashed lines.

undeformed triangular element. The model parameters were chosen to be $\lambda_{\perp} = 1$, $K/c_0 = 4$, $c_0^*/c_0 = 1$, and $\tau_R = 0.1$. The undeformed, relaxed configuration was used for the initial condition. The material's behavior was tested for the bulk and shear deformation modes. For the triangular element, the deformation modes are shown schematically in Figure 1.8. The bulk and shear deformations of the hexagonal particle were introduced in a similar manner.

The creep behavior of the triangular element was simulated by applying forces of $\|\mathbf{F}\| = 10$ to each of the element nodes, as shown in Figure 1.8. The dynamic equations were then solved to determine the time-dependent strain $\epsilon(t)$; the results are shown in Figure 1.9a. The shear strain is indicated by the solid line and was defined as $\epsilon_{sh}(t) = \tan \gamma(t)$, where γ is the shear angle (see Figure 1.8a). The bulk strain is shown by the dashed line, and was calculated as $\epsilon_b(t) = A(t)/A_0 - 1$, where $A(t)$ and A_0 are the element areas in the deformed and undeformed states, respectively. Figure 1.9a demonstrates that, due to the viscoelasticity of the material, the application of the external force leads to a gradual build-up of the strain.

The stress relaxation behavior of the triangular element was obtained by determining the forces that develop in the material after an instantaneous deformation, which then is kept constant. Figure 1.9b shows the results of simulations at the instantaneous shear and bulk strains of $\epsilon_{sh} = 0.207$ and $\epsilon_b = 0.718$, respectively. Figure 1.9b shows that the nodal force, $F(t)$, acquires its maximum value $F(0)$ at an initial moment of deformation, and then decreases as the viscoelastic relaxation takes place. It can be seen in Figure 1.9b that the shear stress relaxation is noticeably stronger than the bulk stress relaxation.

When six triangular elements are put together to form a hexagonal particle, the resulting particle “inherits” the viscoelastic properties of the constituent elements. Figure 1.10 shows the creep behavior of the hexagonal particle after the shear and bulk stresses are applied. To model the creep behavior under shear, the two bottom nodes were pinned to their equilibrium positions, the shear forces of $\|\mathbf{F}\| = 10$ were applied to the two top nodes, and the particle height and distance between the

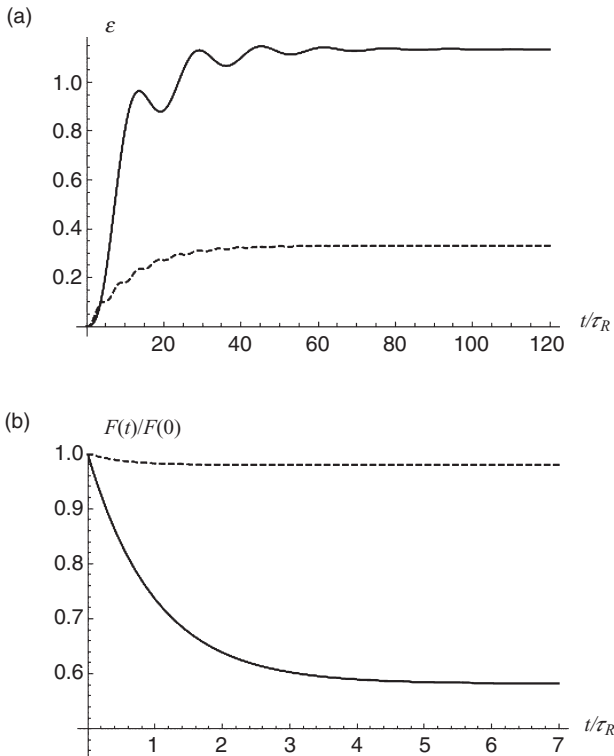


Figure 1.9 (a) Creep and (b) stress relaxation of a triangular element under the shear (solid curves) and bulk (dashed curves) deformations (see text for notations); τ_R is the relaxation time, as defined in Equation 1.15.

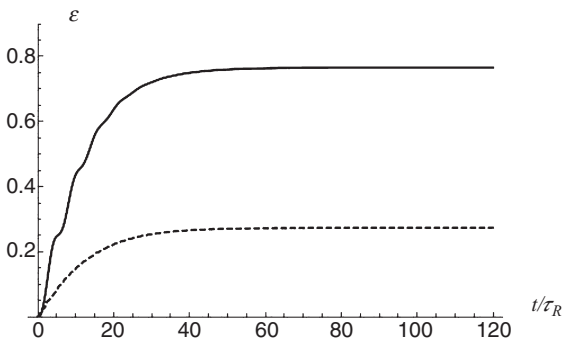


Figure 1.10 Creep behavior of a hexagonal nanogel particle (Figure 1.7a) under the shear (solid curve) and bulk (dashed curve) modes of deformation.

top nodes were kept constant. The creep behavior under dilatation was modeled by applying the pressure of $p = 10$ that pulls the surface nodes outwards. (The pressure p was computed as the value of the applied force divided by the current length of an edge.) By comparing Figures 1.9a and 1.10, it can be seen that the individual triangular elements and the hexagonal particle exhibit similar viscoelastic behaviors.

The approach outlined above provides a powerful method for modeling the behavior of deformable materials that encompass viscoelastic behavior. In future studies, this model will be built on to determine how the viscoelasticity of the nanogels affects the macroscopic response of the dual crosslinked material described in this chapter.

1.4

Conclusions

To summarize, the aim of the present studies was to demonstrate how computational modeling can be used to design self-healing materials and coatings. To that end, previous studies on nanoscopic gel particles that are interconnected into a microscopic network by both stable and labile bonds were reviewed. New calculations for modeling the viscoelastic behavior of the individual nanogel particles were also described.

To demonstrate the self-healing behavior of dual crosslinked polymeric materials, the response of a network of deformable nanogels to a tensile stress was modeled; this showed that the introduction of a small fraction of labile crosslinks can lead to dramatic improvements in the strength of a material. The rapid reforming of these labile bonds provides the structural rearrangement that preserves the mechanical integrity of the sample.

Analogies can be drawn with other experimental systems that indicate the validity of these predictions. For example, it is useful to recall the polydisulfide chains that contribute to the unique properties of rubber [39]. In particular, the reshuffling of the labile S–S bonds in the polysulfide crosslinks as the rubber is deformed is what contributes to the toughness of this material [40]. Recently, investigations have shown that polymer chains which encompass a significant fraction of hydrogen bonds can also undergo a rapid structural rearrangement due to bond breaking and remaking that imparts self-healing properties to the bulk material [3].

Acknowledgments

The authors gratefully acknowledge financial support from the DOE (for partial support of G.V.K. and S.F.D.), and ONR (for the partial support of V.V.Y.). G.V.K. also acknowledges partial support from NSF through TeraGrid resources provided by NCSA.

References

- 1 Caruso, M.M., Davis, D.A., Shen, Q., Odom, S.A., Sottos, N.R., White, S.R. and Moore, J.S. (2009) Mechanically-induced chemical changes in polymeric materials. *Chemical Reviews*, **109**, 5755–98.
- 2 Chen, X., Dam, M.A., Ono, K., Mal, A., Shen, H., Nutt, S.R., Sheran, K. and Wudl, F.A. (2002) Thermally re-mendable cross-linked polymeric material. *Science*, **295**, 1698–702.
- 3 Cordier, P., Tournilhac, F., Soulie-Ziakovic, C. and Leibler, L. (2008) Self-healing and thermoreversible rubber from supramolecular assembly. *Nature*, **451**, 977–80.
- 4 Amendola, V. and Meneghetti, M. (2009) Self-healing at the nanoscale. *Nanoscale*, **1**, 74–88.
- 5 Trask, R.S., Williams, H.R. and Bond, I.P. (2007) Self-healing polymer composites: mimicking nature to enhance performance. *Bioinspiration and Biomimetics*, **2**, P1–9.
- 6 Balazs, A.C. (2007) Modeling self-healing materials. *Materials Today*, **10**, 18–23.
- 7 Wool, R.P. (2008) Self-healing materials: a review. *Soft Matter*, **4**, 400–18.
- 8 Wu, D.Y., Meure, S. and Solomon, D. (2008) Self-healing polymeric materials: a review of recent developments. *Progress in Polymer Science*, **33**, 479–522.
- 9 Hickenboth, C.R. *et al.* (2007) Biasing reaction pathways with mechanical force. *Nature*, **446**, 423–7.
- 10 Kolmakov, G.V., Matyjaszewski, K. and Balazs, A.C. (2009) Harnessing labile bonds between nanogel particles to create self-healing materials. *ACS Nano*, **3**, 885–92.
- 11 Min, K. and Matyjaszewski, K. (2005) Atom-transfer radical atom polymerization in microemulsion. *Macromolecules*, **38**, 8131–4.
- 12 Min, K., Gao, H. and Matyjaszewski, K. (2006) Development of an ab initio emulsion transfer radical polymerization: from microemulsion to emulsion. *Journal of the American Chemical Society*, **128**, 10521–6.
- 13 Smith, B.L., Schaffer, T.E., Viani, M., Thompson, J.B., Frederick, N.A., Kindt, J., Belcher, A., Stucky, G.D., Morse, D.E. and Hansma, P.K. (1999) Molecular mechanistic origin of the toughness of natural adhesive, fibres and composites. *Nature*, **399**, 761–3.
- 14 Kolmakov, G.V., Revanur, R., Tangirala, R., Emrick, T., Russell, T.P., Crosby, A.J. and Balazs, A.B. (2010) Using nanoparticle-filled microcapsules for site-specific healing of damaged substrates: creating a “repair-and-go” system. *ACS Nano*, **4**, 1115–23.
- 15 Therriault, D., White, S.R. and Lewis, J.A. (2003) Chaotic mixing in three-dimensional microvascular networks fabricated by direct-write assembly. *Nature Materials*, **2**, 265–71.
- 16 Ashurst, W.T. and Hoover, W.G. (1976) Microscopic fracture studies in the two-dimensional triangular lattice. *Physical Review B*, **14**, 1465–73.
- 17 Buxton, G.A., Care, C.M. and Cleaver, D.J. (2001) A lattice spring model of heterogeneous materials with plasticity. *Modelling and Simulation in Materials Science and Engineering*, **9**, 485–97.
- 18 Buxton, G.A. and Balazs, A.C. (2004) Modeling the dynamic fracture of polymer blends processed under shear. *Physical Review B*, **69**, 054101.
- 19 Yashin, V.V. and Balazs, A.C. (2006) Pattern formation and shape changes in self-oscillating polymer gels. *Science*, **314**, 798–801.
- 20 Kuksenok, O., Yashin, V.V. and Balazs, A.C. (2007) Mechanically induced chemical oscillations and motion in responsive gels. *Soft Matter*, **3**, 1138–44.
- 21 Bell, G.I. (1978) Models for the specific adhesion of cells to cells. *Science*, **200**, 618–27.
- 22 Chang, K.C., Tees, D.F.J. and Hammer, D.A. (2000) The state diagram for cell adhesion under flow: leukocyte rolling and firm adhesion. *Proceedings of the National Academy of Sciences of the United States of America*, **97**, 11262–7.
- 23 Wiita, A.P., Ainarapu, S.R.K., Huang, H.H. and Fernandez, J.M. (2006) Force-dependent chemical kinetics of disulfide bond reduction observed with

- single-molecule techniques. *Proceedings of the National Academy of Sciences of the United States of America*, **103**, 7222–7.
- 24** Bell, G.I., Dembo, M. and Bongrand, P. (1984) Cell adhesion. Competition between nonspecific repulsion and specific bonding. *Biophysical Journal*, **45**, 1051–64.
- 25** King, M.R. and Hammer, D.A. (2001) Multiparticle adhesive dynamics: hydrodynamic recruitment of rolling leukocytes. *Proceedings of the National Academy of Sciences of the United States of America*, **98**, 14919–24.
- 26** Bhatia, S.K., King, M.R. and Hammer, D.A. (2003) The state diagram for cell adhesion mediated by two receptors. *Biophysical Journal*, **84**, 2671–90.
- 27** Sanderson, R.T. (1976) *Chemical Bonds and Bond Energy*, 2nd edn, Academic Press, New York.
- 28** Lawn, B.R. (1993) *Fracture of Brittle Solids*, 2nd edn, Cambridge University Press, New York.
- 29** Dirama, T.E., Varshney, V., Anderson, K.L., Shumaker, J.A. and Johnson, J.A. (2008) Coarse-grained molecular dynamics simulations of ionic polymer networks. *Mechanics of Time-Dependent Materials*, **12**, 205–20.
- 30** Tsige, M., Lorentz, C.D. and Stevens, M.J. (2004) Role of network connectivity on the mechanical properties of highly cross-linked polymers. *Macromolecules*, **37**, 8466–72.
- 31** Budinski, K.G. and Budinski, M.K. (2004) *Engineering Materials: Properties and Selection*, 8th edn, Prentice-Hall, Columbus.
- 32** Mukherji, D. and Abrams, C.F. (2008) Microvoid formation and strain hardening in highly cross-linked polymer networks. *Physical Review E*, **78**, 050801(R).
- 33** Gents, A.N. (1994) Strength of elastomers, *Science and Technology of Rubber*, 2nd edn (eds J.E. Mark, B. Erman and F.R. Eirich), Academic Press, New York, pp. 471–512.
- 34** Yashin, V.V. and Balazs, A.C. (2007) Theoretical and computational modeling of self-oscillating polymer gels. *Journal of Chemical Physics*, **126**, 124707.
- 35** Atkin, R.J. and Fox, N. (1980) *An Introduction to the Theory of Elasticity*, Longman, New York.
- 36** Drozdov, A.D. (1996) *Finite Elasticity and Viscoelasticity: A Course in the Nonlinear Mechanics of Solids*, World Scientific, Singapore.
- 37** Bonet, J. and Wood, R.D. (1997) *Nonlinear Continuum Mechanics for Finite Element Analysis*, Cambridge University Press, New York.
- 38** Zienkiewicz, O.C. (1977) *The Finite Element Method*, 3rd edn, McGraw-Hill, London.
- 39** Tobolsky, A.V. and MacKnight, W.J. (1965) *Polymeric Sulfur and Related Polymers*, Wiley-Interscience, New York.
- 40** Aklonis, J.J. and McKnight, W.J. (1983) *Introduction to Polymer Viscoelasticity*, 2nd edn, Wiley-Interscience, New York.